Nonlinear dynamics of bistable composite cantilever shells: an experimental and modelling study

Matteo Brunetti[a,], Andrzej Mitura[b], Francesco Romeo[c], Jerzy Warminski[b]

[a]*Department of Civil and Industrial Engineering, University of Pisa, Largo Lazzarino 1, 56122, Pisa, Italy*
[b]*Department of Applied Mechanics, Lublin University of Technology, Nadbystrzycka 36, 20-618, Lublin, Poland*
[c]*Department of Structural and Geotechnical Engineering, University of Roma La Sapienza, via Eudossiana 18, 00184, Rome, Italy*

Abstract

The nonlinear dynamics of cantilever bistable shells with asymmetric stable configurations is investigated. The possibility of maximising the kinetic energy associated with snap-through motion offered by the considered cantilevered shells is pursued to enhance the sought-after energy harvesting capabilities. Through an experimental campaign under harmonic forcing the resonance scenarios around the stable configurations are analysed. The resulting nonlinear behaviour observed for high amplitude excitation is adopted to guide a reduced order model derivation. By combining the experimental response with two double-well oscillators derived from FE simulations, a double-well quintic oscillator capturing the observed softening behaviour is proposed. It involves a parameter identification phase in which a nonlinear damping model is introduced. A numerical continuation approach is adopted to discuss the local periodic solutions around each stable configuration in terms of resonance curves, bifurcation diagrams and basins of attraction. The global dynamics involving regular and chaotic dynamic regimes as well as snap-through motion is eventually described.

Email addresses: matteo.brunetti@unipi.it (Matteo Brunetti), a.mitura@pollub.pl (Andrzej Mitura), francesco.romeo@uniroma1.it (Francesco Romeo), j.warminski@pollub.pl (Jerzy Warminski)

1. Introduction

The possibility of designing and manufacturing structures characterized by intentional multistable behaviour raises considerable interest for both technological and scientific reasons. Their applications range nowadays from aerospace to energy harvesting industries in which the morphing capabilities arising from the presence of more equilibrium positions are exploited in different ways. By restricting ourselves to bistable structures, the coexistence of two stable configurations can be ascribed to several effects. For unsymmetric composite laminates, mechanical bistability due to curing thermal residual stresses was observed by Hyer forty years ago [1]. As shown in [2], the introduction of residual bending stresses in thin, homogeneous, isotropic leads to stable configurations with curvatures of opposite sign. By applying a prestress to selected fibres, bistable behaviour can also be obtained for laminates with a symmetric layup [3]. Fibre-reinforced composites can also induce bistability in thin cylindrical shell structures: either a tight coil or helical second stable configuration is obtained for antisymmetric and symmetric layup, respectively [4]. Multistable shells can also be obtained by mechanically inducing a prestress on a initially curved stress free configuration. This makes it easy to design multistable shells with boundary constraints [5, 6, 7]. A special class of cantilever composite shells exhibiting multi-stability has been presented by the authors in [8]. Finite element numerical simulations confirmed by experimental tests demonstrated the existence of two or four stable equilibrium configurations, depending on the shape of the natural stress-free configuration of the shell. More recently, the cantilevered configuration was also studied in [9] to obtain snap-through characteristics and design criteria for bistable laminates with carbon-epoxy and glass-epoxy layers. Comprehensive literature reviews on bistable composite laminates can be found in [10, 11].

Irrespective of the source of mechanical bistability, the force required for snapthrough motion can be reduced by dynamically driving the structure's change of configuration. Therefore, in the last ten years numerous theoretical and experimental studies have been devoted to describe and possibly exploit the bistable behaviour under dynamic actuation. In [12] the snap-through dynamics of cross-ply laminated composite bistable plates was studied for square and rectangular geometries. The nonlinear behaviour of a square bistable laminate excited by a shaker acting at the center of the plate was studied in [13] addressing the so-called *in-well* dynamic regimes, that is, the

ones occuring when the shell oscillates around one of the two stable equilibria. A low order model, whose coefficients were identified from the experimental frequency response, was adopted to capture the subharmonic behaviour and estimate the stability boundaries; the model involves quadratic nonlinearities for both the restoring force and the modal coupling term. The latter model was then extended by including a frequency dependent displacement threshold beyond which snap-through was experimentally observed [14]. This allowed to address the so-called *cross-well* dynamic regimes, that is, the ones occuring when the shell oscillates back-and-forth between the two stable equilibria. A two-way actuation through piezoelectric patches (MFC) of dynamic morphing was proposed in [15]; the dynamic snap-through was obtained by carefully tuning the excitation frequencies for each stable state and by adding point masses. In [16] the linear free vibrations around a stable position of a cross-ply laminate were studied. A bistable cantilever unsymmetric laminate was investigated in [17] to achieve full-state configuration control by inducing and reversing snap-through as desired. Besides the experimental investigations, a number of studies focused on the modelling aspects required to predict and interpret the nonlinear dynamics of bistable composite laminates under harmonic excitation. The response for the transverse displacement was obtained in [18] following a Rayleigh–Ritz–Galerkin approach. To take into account the non-constant curvatures, fourth-order polynomials for the out-of-plane displacement field were proposed as shape functions in [19]. More recently, an analytical dynamic model with 17 unknown terms based on Rayleigh's method and Hamilton's principle was proposed in [20]. Provided that the material properties and dimensions are known, the latter model enables the prediction of the nonlinear dynamic response over the entire region of bistable plates. A simplified model depending on only four time-dependent parameters was validated and used in [21] to examine the static and free vibration response of cylindrical bistable laminates with high length-to-thickness ratio.

The dynamics of bistable composite laminates plays a key role for energy harvesting purposes; in particular, to generate electrical energy from ambient vibrations. In this context, bistability, with the ensuing large strain associated with snap-through mechanisms, has shown to significantly enlarge the harvesting frequency bandwidth. In addition, the involved nonlinearities trigger advantageous dynamic regimes in which large amplitude oscillations can be obtained from relatively small input energy. In [22] a square plate with piezoelectric patches was experimentally investigated showing that large

average power was harvested from intermittency, limit cycle and chaotic oscillations for responses with initial condition on both stable states. Energy harvesting performance of bistable composite plates with bonded piezoelectric elements was also investigated in [23, 24, 25]. In these studies, the energy extraction optimization problem was tackled, from a static perspective, by considering the actuation arrangement, the laminate aspect ratio as well as the ply thickness and orientation. A square laminate mounted on the shaker at its center was considered showing that power generation achieved via conventional resonant systems can be improved by relying on repeatable snap-through motion. The energy harvesting capability of a cantilever bistable asymmetric laminates coupled to piezoelectric materials was studied in [26]; at low frequency and low excitation, higher power output over a broader range of frequencies was obtained for the bistable case with respect to its linear counterpart. In [27] the dynamics of a square bistable laminate with piezoelectric layers was successfully predicted by an analytical model characterized by fourth-order shape functions. Under high amplitude excitation, the nonlinear response of the laminate was predicted in [28] by numerically solving the electromechanically coupled equations of motion derived from Lagrange's equations and the Rayleigh-Ritz method.

Most of the studies so far devoted to the dynamics of bistable laminates were characterized by symmetric stable configurations with free boundaries. Although this choice grants clear benefits from an experimental, analytical and modeling point of view, it restricts the geometric shapes of the stable states that can be obtained. This might in turn limit the possibility of maximising the kinetic energy associated with snap-through motion, a necessary condition for optimal energy harvesting performance. To overcome these limitations, a bistable laminate with remarkably different stable geometric configurations is here considered. By extending the authors' previous work [8], the dynamic analysis of a cantilever shell whose design was driven by a semi-analytical model under static loading conditions is theoretically and experimentally investigated. It is worth emphasizing that the considered asymmetry of the clamped stable states stems from the peculiar curved stress-free configuration of the laminate and from the chosen boundary conditions which introduces significant novelties with respect to the cantilever bistable laminates obtained from flat plates (e.g. [15, 17, 25]). In particular, the obtained stable configurations are characterized by remarkably different stored elastic energies and spectral properties. Therefore, the interest lies in studying the large amplitude nonlinear behaviour of such a class of shells

and possibly exploit this 'asymmetry' for energy harvesting purposes once the snap-through mechanism is triggered.

The paper is organized as follows. In Section 2 the key geometric and constitutive features of the class of cantilever bistable shells considered in this study are introduced. In Section 3 the experimental campaign under harmonic forcing is reported; it focuses on the resonance scenarios around the stable configurations and the nonlinear behaviour observed for high amplitude excitation. Next, in Section 4, the reduced order model derivation is discussed. Driven by the experimental evidence and two double-well oscillators derived from FEM simulations a double-well quintic oscillator is derived. The involved parameter identification is also described in which the key role played by damping modelling is highlighted. The nonlinear dynamics main features are presented in Section 5 by addressing at first the periodic behaviour around each stable configuration in terms of resonance curves, bifurcation diagrams and basins of attraction. Then, the global dynamics involving regular and chaotic dynamic regimes as well as snap-through motion is described prior to the concluding remarks.

2. Cantilever bistable shells with asymmetric stable configurations

We consider the class of cantilever multistable shells proposed in [5, 6] and numerically and experimentally investigated in [8]. Starting from a composite shell with rectangular planform and pseudo-conical stress-free shape, a cantilevered multistable shell is obtained by inducing a prestress by flattening and clamping one of its short edges. The multistability properties of such a structure (that is, the number of clamped stable configurations, their shapes, elastic energy content, natural frequencies, etc.) depend on its stress-free shape, the constitutive properties of the elementary lamina and the lamination sequence. Here we limit ourselves to the subfamily of multistable shells obtained by choosing (once and for all) the stress-free shape represented in Fig. 1, the elementary lamina whose properties are reported in Tab. 1 and the lamination sequence $[\alpha/-\alpha_2/\alpha/-\alpha/\alpha_2/-\alpha]$, with α measured with respect to the $x-$axis. In this case the multistability properties depend on a single parameter, namely the lamination angle α. The latter can be selected based on the performance requirements of the device to be designed. For the chosen stress-free shape and elementary lamina, the shell, once flattened and clamped to the $x = 0$ edge, turns out to be bistable whenever $\alpha \in [35°, 60°]$. This range, previously estimated by the reduced order

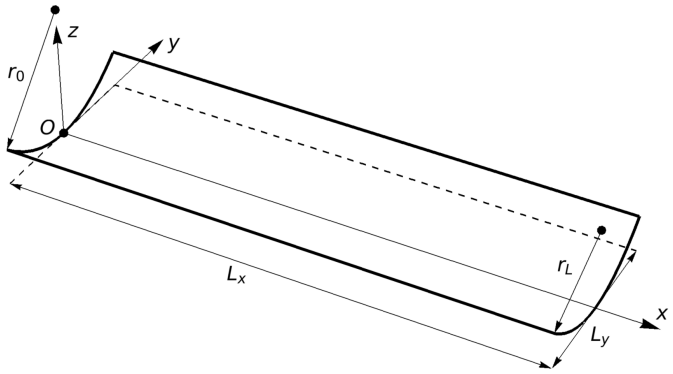

Figure 1: Stress-free shape $z_0(x, y) = [1/r_0 + (1/r_0 - 1/r_L)x/L_x)y^2/2$, where $L_x = 0.45\,\mathrm{m}$, $L_y = 0.15\,\mathrm{m}$, $r_0 = 0.114\,\mathrm{m}$, $r_L = 0.07\,\mathrm{m}$.

ρ (g/mm^3)	E_1 (GPa)	E_2 (GPa)	ν_{12} -	G_{12} (GPa)	G_{13} (GPa)	G_{23} (GPa)	t_ℓ (mm)
1.996	130.71	6.36	0.32	4.18	4.18	0.1	0.145

Table 1: Elementary lamina: unidirectional carbon/epoxy composite data (M12/35%/UD134/AS7/300).

model proposed in [5, 6], has been verified via finite element (FE) simulations carried out using the commercial software *Abaqus*.

The FE model has been developed by taking advantage of the *Python* scripting interface. The stress-free shape of the shell has been created starting from spline approximations of the curved edges and using the *shell loft* feature to generate the middle surface; the laminate has been defined using the composite layup functionality with 3 integration points per ply. We used general purpose *S4R* shell elements with reduced integration.

For each choice of the lamination angle α within the bistable domain, let C_1^α be the stable configuration that the shell naturally assumes soon after clamping, that is, its first stable configuration, and C_2^α be its second stable configuration. Each numerical simulation consists of 3 steps: at first, the C_1^α configuration is obtained by flattening and clamping the $x = 0$ edge (*step 1*); then, a follower force is applied at the shell tip to trigger the switch towards the C_2^α configuration (*step 2*); finally, the force is released to check whether the shell settles to the C_2^α configuration (*step 3*). We use a *Static, General* procedure for all steps. Fig. 2 shows the shape, the elastic energy content and angular frequency of the first mode for both the C_1^α, C_2^α configurations as the lamination angle varies. As can be seen, for $\alpha \simeq 45°$ a drastic change in the shape of the second stable configuration C_2^α is observed, resulting in a sudden change in its stored elastic energy and angular frequency. This is due to the fact that an increase in the lamination angle corresponds to a decrease in the ratio between longitudinal and transverse stiffnesses which favors the stability of configurations with large longitudinal curvature and small (or even vanishing) transverse curvature. The value of the lamination angle at which this occurs depends on the properties of the specific lamina. By taking into account the expected energy and spectral features of the two configurations, the design possibilities while searching for the optimal harvesting performance are enlarged. Being interested in studying the nonlinear dynamics of bistable shells with *widely differing* stable configurations, in the following we investigate the case $\alpha = 45°$; in the remainder of the paper, due to the shapes assumed by the shell, the C_1^{45}, C_2^{45} configurations are renamed I, C, respectively. As shown in Fig. 2d, this specific choice of lamination angle entails that both the elastic energy gap between I and C configurations and the longitudinal curvature of C are maximal. Moreover, it can be observed that the difference between the frequency of the first mode of vibration between the two stable configurations, albeit not maximal, is large enough to give rise to resonant dynamics for rather distinct forcing frequen-

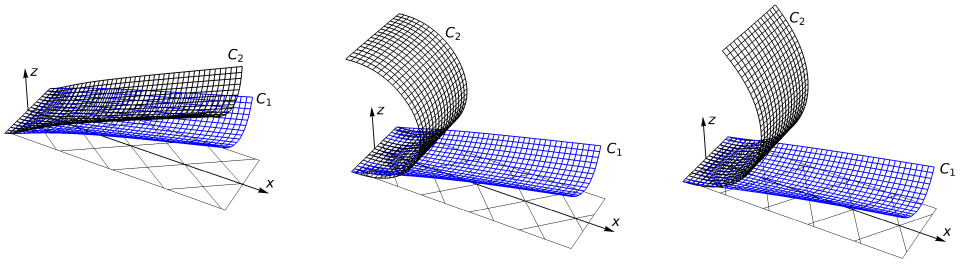

(a) $\alpha = 35°$. (b) $\alpha = 45°$. (c) $\alpha = 55°$.

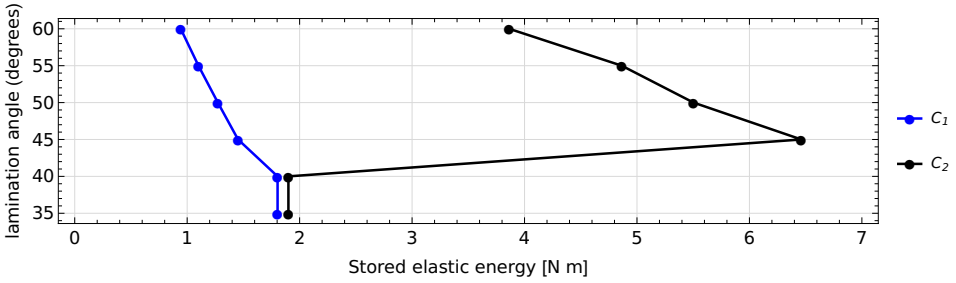

(d) Elastic energies

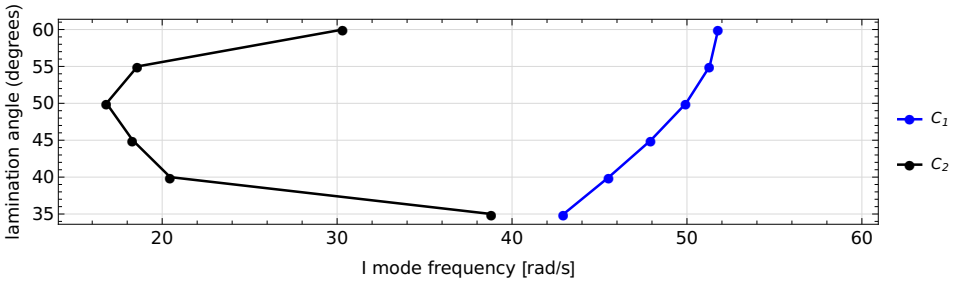

(e) Frequencies

Figure 2: Shapes, elastic energies and frequencies of the clamped shell stable configurations as the lamination angle α varies.

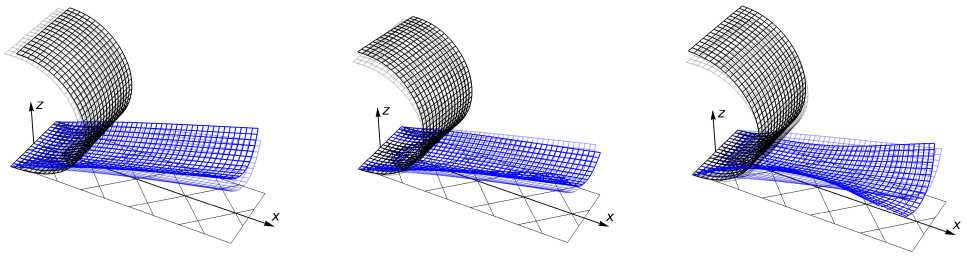

(a) M1 ($\omega_I = 49.7\,\text{rad/s}$, $\omega_C = 18.3\,\text{rad/s}$). (b) M2 ($\omega_I = 248.2\,\text{rad/s}$, $\omega_C = 57.4\,\text{rad/s}$). (c) M3 ($\omega_I = 785.5\,\text{rad/s}$, $\omega_C = 82.0\,\text{rad/s}$).

Figure 3: First three natural modes for I and C configuration ($\alpha = 45°$).

cies, Fig. 2e. Fig. 3 shows the angular modal frequencies, namely ω_I, ω_C, for the I and C configurations, respectively; in this study, being interested in high amplitude motion, the dynamic actuation of the bistable shell focuses on the first mode of vibration for both the configurations.

3. Experimental campaign under harmonic excitation

3.1. Shell sample and experimental setup

The shell was formed using a single-sided aluminium mould specifically designed according to the geometry of the stress-free shape (see Fig. 1); we refer to [8] for all the details about the manufacturing process. Then, the curved edge having smaller curvature (i.e. r_0) was flattened and forced to remain flat between two clamps fixed to the shaker. As a result of this clamping action, the shell settles in the so-called I configuration (Fig. 4a); starting from such configuration, to make the shell settle in the C configuration (Fig. 4b), as described in Section 2, a quasi-static external actuation is provided.

The shell dynamic behaviour was investigated by experimental tests performed using a *59335 Tira* electrodynamic shaker. A 3-axis accelerometer, glued close to the middle of the shell free edge, was used to acquire measurements during forward and backward frequency sweeps. A *LMS vibration analyzer* was used to integrate the signals and calculate the displacement amplitudes in both the x and z (global) sensor directions.

3.2. Small oscillations behaviour

The shell's small oscillations around the two stable configurations were investigated by performing backward and forward frequency sweeps of con-

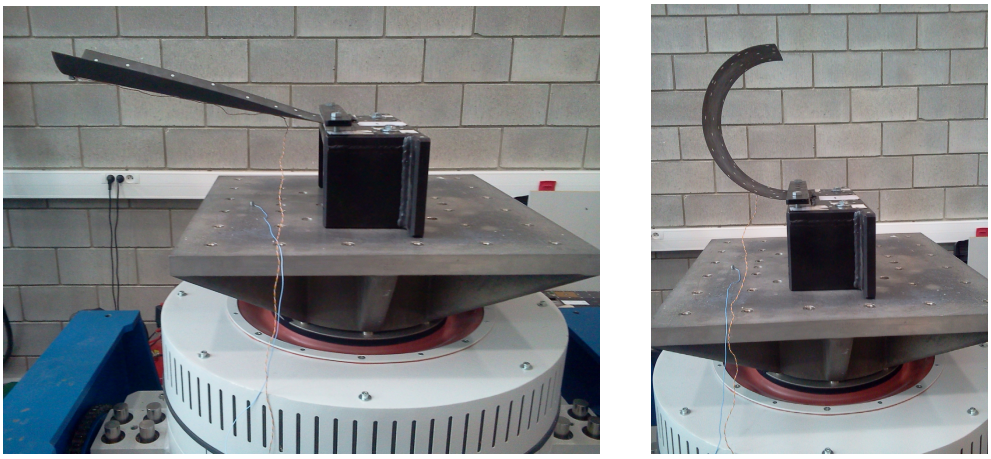

(a) I shape. (b) C shape.

Figure 4: Shell clamped stable configurations.

stant amplitude ($a_s = 0.1$ g) harmonic base acceleration. Fig. 5 shows the experimental results for both the I (blue) and C (black) stable configurations in terms of the displacement amplitudes in the x (Fig. 5a) and z (Fig. 5b) global directions; continuous and dashed lines correspond to forward and backward frequency sweep measurements, respectively.

As shown in Fig. 5, the angular frequencies of the first mode of vibration near the stable configurations are found to be $\omega_I \approx 43.5\,\mathrm{rad/s}$ and $\omega_C \approx 28.9\,\mathrm{rad/s}$. We remark that these values differ from those obtained with the FE model (see Fig. 3), the difference being due to the unavoidable imperfections introduced by the manufacturing process and the clamping boundary condition. In particular, the clamp of the experimental device does not guarantee a complete flattening of the (initially) curved edge. Such difference was easily removed by assigning to the clamp of the FE model a slight residual curvature ($\approx 5\%$ of the initial curvature $1/r_0$). The resonance curves show that the first mode vibrations mostly involve either the vertical or the horizontal component of the motion for the I and the C configuration, respectively. For the same harmonic forcing, the amplitude of oscillations of the I configuration is larger than the C one and the width of the resonance curves indicates a different damping scenario for the two cases; the significant latter aspect deserves attention and is dealt with in a later section.

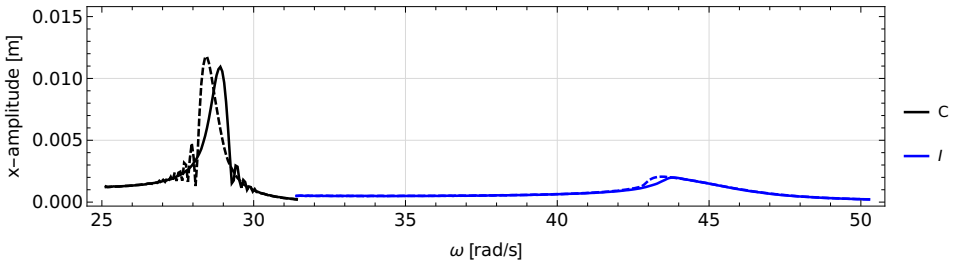

(a) x-amplitude.

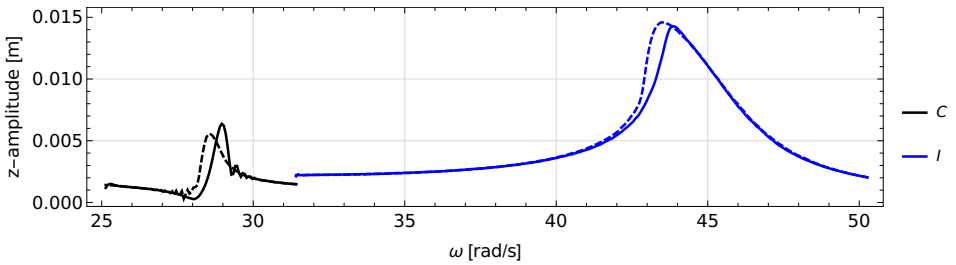

(b) z-amplitude.

Figure 5: Small oscillations dynamic response of the shell near the I and C configurations, backward (dashed line) and forward (continuous line).

3.3. Large oscillations behaviour

The shell's large oscillations were investigated by repeating backward and forward frequency sweeps for increasing values of the harmonic base acceleration $a_s = \{0.1, 0.5, 1.0, 1.5\}$ g. Fig. 6 shows the experimental results obtained when the sweep is applied to the shell settled in the I (blue) and C (black) configurations, respectively.

The motion components for the two configurations as well as the amplitude of oscillations follow the small amplitude case. For both configurations, as the amplitude increases the resonant frequency shifts towards lower frequencies. This softening behavior is more evident when the sweep is carried out starting with the shell settled in the I configuration. For the latter, the clear jump in the higher forcing amplitude resonance curve indicates the presence of an unstable branch.

3.4. Damping identification

For an accurate damping identification, a high-speed camera with its optical axis perpendicular to the vibrating shell was adopted. The recorded data allowed determining the vertical (z) and horizontal (x) components of

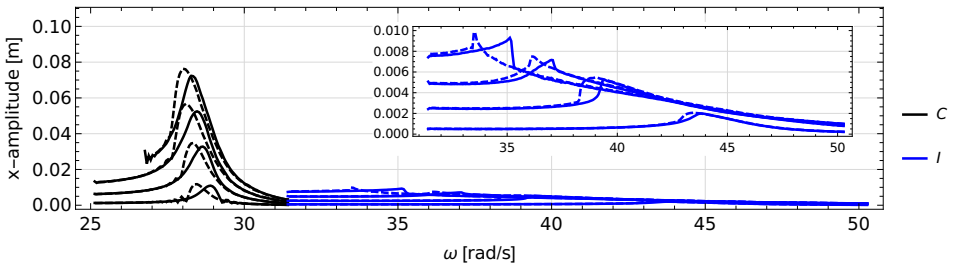

(a) x-amplitude.

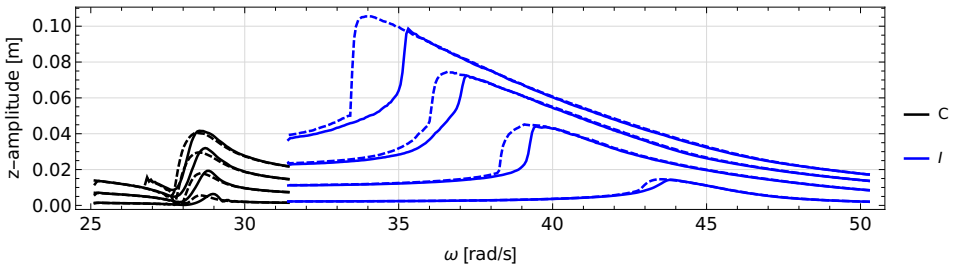

(b) z-amplitude.

Figure 6: Large oscillations dynamic response of the shell starting from the I and C stable configurations, backward (dashed line) and forward (continuous line).

displacement and velocity of the shell free end; samples of free vibrations time series for the x and z components around the I and C configurations are shown in Fig. 7.

As shown in Fig. 8, the velocity time series determined experimentally for small and large natural oscillations are characterized by a significantly different amplitude envelopes. Therefore, a linear damping term in the reduced order model is considered inadequate. In particular, for the I configuration (C configuration) the viscous damping coefficient estimated from large amplitude oscillations is about 2.5 times higher (2 times higher) than the one obtained for small amplitude oscillations. The results clearly show that the damping model should be dependent on vibrations level. The shell has a substantial surface area and air resistance can be significant, so, as proposed in [29], a quadratic term is introduced in addition to the linear one. In the following, the identification of the coefficients of both terms (linear or nonlinear) obtained from forced vibration will be described. Besides the air resistance, the identified damping model allows to take into account different damping mechanisms occurring during the experimental tests, such as

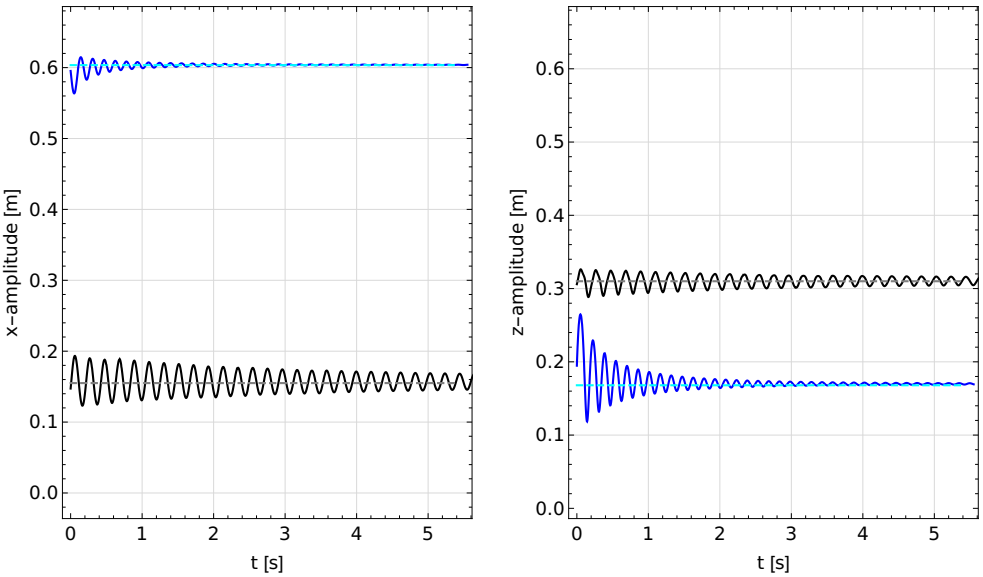

(a) x-amplitude. (b) z-amplitude.

Figure 7: Experimental time series (I, blue; C, black). The dashed lines specify the reference position of the point at the free end of the shell in the two stable configurations.

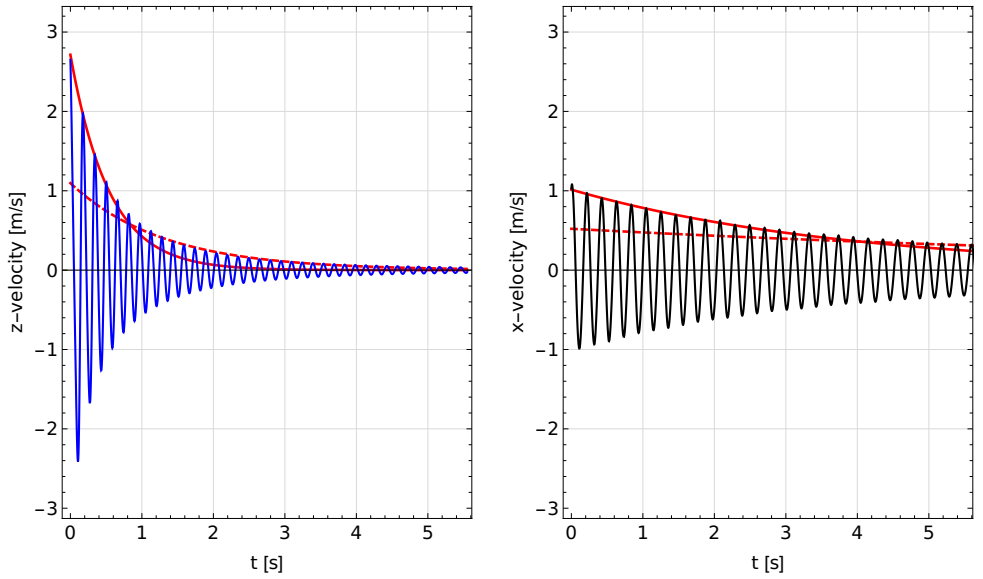

(a) $I-$configuration (b) $C-$configuration

Figure 8: Velocity time series and amplitude envelopes for small (red dashed lines) and large oscillations (red continuous lines).

internal material damping and clamps dry friction.

4. Reduced order model derivation

In this section the derivation of a reduced order model enabling to retrace the observed rich experimental dynamics of the bistable shell under investigation is presented. Such derivation comprises the choice of tractable suitable models and the identification of the relevant parameters. The process was divided into two phases. Firstly, the dynamics of each configurations is described separately using the Duffing-Holmes model. Then the description of both oscillators is combined into one global model.
Being in presence of a clear softening effect and vibration offset a Duffing-Holmes model is adopted with the following differential form:

$$\ddot{q}_i + \kappa_{1i} q_i + \kappa_{3i} q_i^3 + \xi_{1i} \dot{q}_i + \xi_{2i} \dot{q}_i |\dot{q}_i| = \mu_i \lambda g \sin(\omega t) \qquad i = I, C \tag{1}$$

where q_i are generalized coordinates independently describing the shell vibration around both equilibria. Depending on the configuration for which the vibrations are considered the subscript i can take I or C notation. In this model the nonlinear restoring force is given by the sum of linear and cubic terms, with negative κ_{1i} and positive κ_{3i} terms. According to the observed damping experimental features, a viscous damping with linear parameter ξ_{1i} and a nonlinear quadratic one ξ_{2i} is assumed. The latter is introduced to take into account the shell surface air resistance which can be significant for high amplitude vibrations. The reduced harmonic forcing proportional to the acceleration λg is rescaled by the coeffcient μ_i. In the model (1), the values of five parameters are unknown, namely $\{\kappa_{1i}, \kappa_{3i}, \xi_{1i}, \xi_{2i}, \mu_i\}$. The parameters $\{\kappa_{1i}, \kappa_{3i}\}$ were identified from the backbone curve, whose analytic expression is determined using the harmonic balance method. Accordingly, for free undamped vibrations and limiting ourselves to the first order approximation, the solution takes the form

$$q_i = A_0 + A_1 \sin(\omega_{0i} t) + A_2 \cos(\omega_{0i} t) \tag{2}$$

where A_1, A_2 are harmonic amplitudes, A_0 is a constant value corresponding to the vibration offset and ω_{0i} are the natural frequencies. The relation between natural frequency and vibration amplitude $A = \sqrt{A_1^2 + A_2^2}$ is given by

$$\omega_{0i}^2 = -2\kappa_{1i} - \frac{15}{4} \kappa_{3i} A^2 \tag{3}$$

Based on the location of the maximum vibration amplitudes on the experimental resonance characteristics, a few points close to the experimental backbone curve were selected. By matching them with the analytical equation (3) the values of κ_{1i} and κ_{3i} coefficients were identified. The remaining parameters ξ_{1i}, ξ_{2i} and μ_i were identified from the comparison of experimental and numerical resonance characteristics. Based on an iterative search, the set of values for damping coefficients and scale factors providing the best fit was determined. In particular, the best set of parameters was the one providing the minimum value of maximum distance (minmax) between the numerical and experimental resonance points. The selected curves for optimal fit are shown in Figures 9-10. The computed parameters values for both configura-

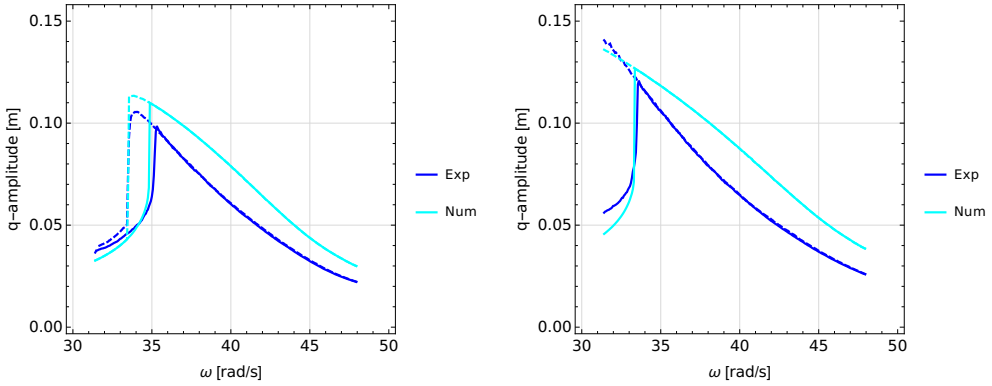

(a) $\lambda = 1.5$ (b) $\lambda = 2.0$

Figure 9: Comparison of experimental and numerical curves, I configuration.

tions are summarized in Table 2; we observe that the negative sign obtained for the k_{1i} parameters is a direct consequence of the bistability of the shell and the Duffing-Holmes model adopted.

i	$\kappa_{1i}(\mathrm{s}^{-2})$	$\kappa_{3i}(\mathrm{m}^{-2}\,\mathrm{s}^{-2})$	$\xi_{1i}(\mathrm{s}^{-1})$	$\xi_{2i}(\mathrm{m}^{-1})$	$\mu_i(-)$
I	-825.96	12560.	1.8847	0.96	1.42
C	-410.	1550.	0.275	0.312	0.12

Table 2: Selected parameters for the two independent Duffing-Holmes oscillators.

Once determined the structure and the parameters of the ideal equivalent oscillators describing the independent dynamics around the two stable shell

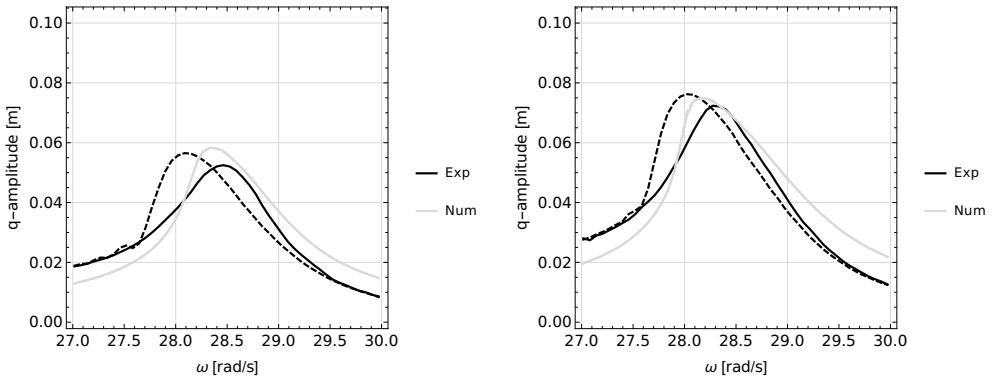

(a) $\lambda = 1.$ (b) $\lambda = 1.5$

Figure 10: Comparison of experimental and numerical curves, C configuration.

equilibria, a global description of the elastic force is pursued. Towards this goal, the attention is shifted to the potential energy associated to the bistable system. Based on the available information from FEM, the potential curve minima corresponding to the equilibrium positions were identified: $V_I \simeq 1.8\,\mathrm{J}$, $V_C \simeq 6.4\,\mathrm{J}$. According to the previous identification phase, in the neighbourhood of these minima the shell dynamics shall be described through the identified stiffness coefficients $(\kappa_{1i}, \kappa_{3i})$. The global generalised coordinate q is shifted so that it takes negative and positive values for configurations I and C, respectively. By labelling the equilibrium positions as $\hat{q}_I$ and $\hat{q}_C$, the conditions to be fulfilled in order to match the potential curve can be written as

$$V = \begin{cases} V_I + m\kappa_{1I}\dfrac{(q-\hat{q}_I)^2}{2} + m\kappa_{3I}\dfrac{(q-\hat{q}_I)^4}{4} & \text{when } |q-\hat{q}_I| < \epsilon_I \\ V_C + m\kappa_{1C}\dfrac{(q-\hat{q}_C)^2}{2} + m\kappa_{3C}\dfrac{(q-\hat{q}_C)^4}{4} & \text{when } |q-\hat{q}_C| < \epsilon_C \end{cases} \tag{4}$$

where parameters ϵ_I and ϵ_C, given by maximum shell deflections observed in the identified Duffing-Holmes oscillators, define the neighbourhood of the equilibrium positions. The obtained description of potential energy provides a global function associated with a single differential equation enabling the approximation of the main nonlinear response features observed during the experimental campaign. The reference potential points from (4) are computed and approximated by means of the polynomial function

$$\tilde{V} = \tilde{V}_0 + \kappa_1\frac{q^2}{2} + \kappa_2\frac{q^3}{3} + \kappa_3\frac{q^4}{4} + \kappa_4\frac{q^5}{5} + \kappa_5\frac{q^6}{6} \tag{5}$$

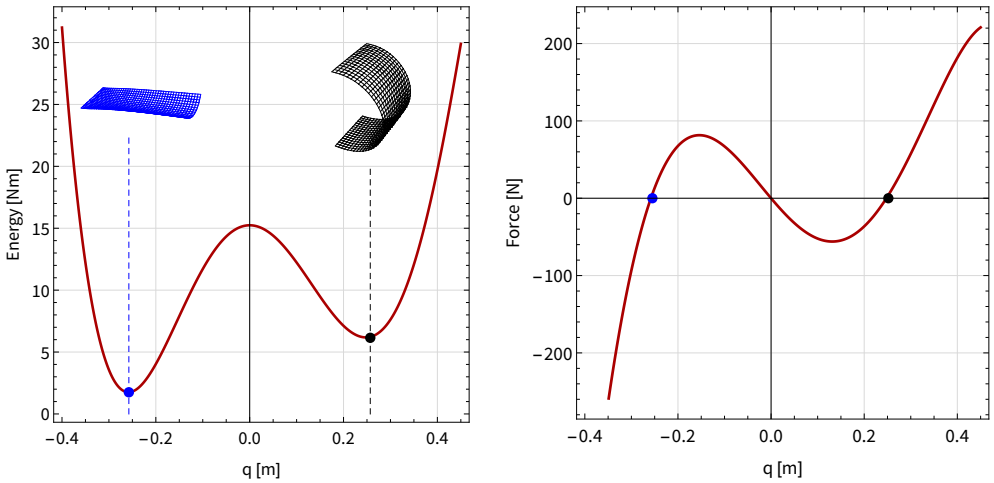

(a) Potential energy. (b) Force.

Figure 11: Potential energy and force of the model.

Finally, the best fit was obtained for the following set of parameters, expressed per unit mass

$$\tilde{V}_0 = 15.24\,\mathrm{m^2 s^{-2}}, \quad \kappa_1 = -712.93\,\mathrm{s^{-2}}, \quad \kappa_2 = 861.81\,\mathrm{m^{-1} s^{-2}},$$
$$\kappa_3 = 11\,813.45\,\mathrm{m^{-2} s^{-2}}, \quad \kappa_4 = -11\,787.63\,\mathrm{m^{-3} s^{-2}}, \quad \kappa_5 = -12\,243.19\,\mathrm{m^{-4} s^{-2}}$$

The obtained double-well potential curve and the corresponding restoring force characteristic are shown in Fig. 11. The resulting analytical nonlinear model takes the form:

$$\ddot{q} + \kappa_1 q + \kappa_2 q^2 + \kappa_3 q^3 + \kappa_4 q^4 + \kappa_5 q^5 + \xi_1 \dot{q} + \xi_2 \dot{q}|\dot{q}| = \mu \lambda g \sin(\omega t) \tag{6}$$

in which the damping coefficients and the scale factors are taken from the identification of the individual oscillators:

$$\xi_1 = \begin{cases} 1.8847\,\mathrm{s^{-1}} & \text{for } q \le 0 \\ 0.275\,\mathrm{s^{-1}} & \text{for } q > 0 \end{cases} \qquad \xi_2 = \begin{cases} 0.96\,\mathrm{m^{-1}} & \text{for } q \le 0 \\ 0.312\,\mathrm{m^{-1}} & \text{for } q > 0 \end{cases}$$
$$\mu = \begin{cases} 1.42 & \text{for } q \le 0 \\ 0.12 & \text{for } q > 0 \end{cases} \tag{7}$$

The accuracy of the proposed model was verified in several ways. Fig. 12 shows the obtained numerical resonance characteristics for different values of

λ, namely 0.1, 0.5, 1, 1.5 and 2 which correspond to the experimental cases. From a qualitative standpoint, the different softening behaviour as well as the amplitude of the generalized displacement for the two configurations matches satisfactorily the experimental results. For I configuration the obtained nat-

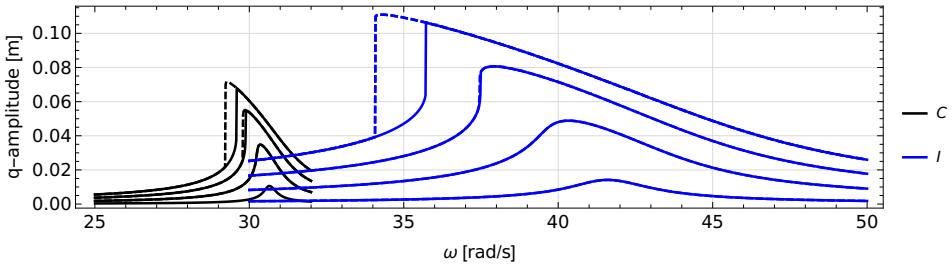

Figure 12: Large oscillations dynamic response obtained from the reduced model, backward (dashed line) and forward (continuous line).

ural frequency is about 6.65Hz and it is slightly lower than the experimental one (6.8 Hz). On the contrary, for C configuration, the natural frequency is about 4.9 Hz and it is slightly larger than the experimental value, namely 4.6 Hz. The numerical and experimental characteristics show a very good agreement around the resonance region for larger vibration amplitude. The maximum error between maximum amplitudes does not exceed 10%.
The obtained reduced nonlinear model captures the shell experimental dynamic features and it will be used in the next section to extend the dynamic analysis to a wider range of amplitudes and frequencies of excitation, via numerical continuation approach.

5. Single-degree-of-freedom model nonlinear dynamics

In this section the nonlinear dynamic regimes of the reduced model (6) are studied as the excitation frequency varies. By selecting this latter as free bifurcation parameter, we use the numerical continuation method provided by the AUTO software ([30]) to detect bifurcations and compute different branches of periodic solutions; direct simulations are performed taking into account local and global dynamics for regular or chaotic oscillations. For the sake of clarity, we recall that λ in the Duffing-Holmes equation (6) is a dimensionless coefficient defining acceleration of excitation in relation to the gravity acceleration g, while μ works as a scaling factor based on the experiment and its value is tuned to experimental data for I and C configuration.

The values of coefficients of the adopted reduced 1 DOF model are summarized in Table 3. The analysis begins from local (in-well) periodic oscillations

Coefficient	**Value**	**Physical unit**
κ_1	-712.93	s^{-2}
κ_2	861.81	$\mathrm{m}^{-1}\mathrm{s}^{-2}$
κ_3	11813.45	$\mathrm{m}^{-2}\mathrm{s}^{-2}$
κ_4	-11787.63	$\mathrm{m}^{-3}\mathrm{s}^{-2}$
κ_5	-12243.19	$\mathrm{m}^{-4}\mathrm{s}^{-2}$
ξ_{1I}	1.8847	s^{-1}
ξ_{2I}	0.96	m^{-1}
μ_I	0.12	[–]
ξ_{1C}	0.275	s^{-1}
ξ_{2C}	0.312	m^{-1}
μ_C	0.12	[–]

Table 3: Value of coefficients of the reduced model.

for I and C configurations.

5.1. Periodic dynamics - I–configuration

The continuation procedure is applied for the I configuration presented in Fig. 4a. Resonance curves presented in Fig. 13 are computed for relatively small amplitudes of excitation: $\lambda = 0.1$, $\lambda = 0.5$, $\lambda = 1$, $\lambda = 1.5$, $\lambda = 2$. The curves are in agreement with the experimental results. The shell oscillates in-well I configuration around ω_{0I} frequency with negative values of coordinate q, see Fig. 11a. The softening effect around natural frequency $\omega \approx \omega_{0I}$ is observed if amplitude of excitation increases and then the unstable solutions occur with the amplitude jump, observed also experimentally. The curves for selected λ values are indicated by different colours (Fig. 13). The jump of amplitude takes place if excitation amplitude λ is greater than 1. Furthermore, apart from the main resonance the subharmonic resonance is observed around half of the natural frequency, $\omega_{0I}/2 \approx 20\,\mathrm{rad/s}$.

The slightly increased value of excitation, up to $\lambda = 2.1$, leads to a period doubling bifurcation, located close to the peak of the resonance curve as presented in Fig. 14a and corresponding zoom, Fig. 14b. We note that the peak of the resonance curve approaches zero value which is close to the limit of the I configuration domain. Time histories for $\omega = 23\,\mathrm{rad/s}$ inside

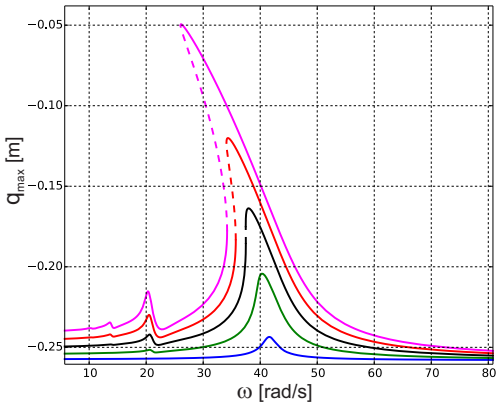

Figure 13: Resonance curves for selected amplitude of excitation $\lambda = 0.1$–blue, $\lambda = 0.5$–green, $\lambda = 1$–black, $\lambda = 1.5$–red, $\lambda = 2.0$–pink; I configuration.

the period doubling zone and for $\omega = 25\,\mathrm{rad/s}$, out of period doubling zone are presented in Fig. 14c.

Blue and green lines correspond respectively to the large and low amplitude branches for $\omega = 23\,\mathrm{rad/s}$, while black and red for $\omega = 25\,\mathrm{rad/s}$. The period doubling bifurcation is indicated by T and $2T$ periods in Fig. 14c.

The narrow zone of the period doubling has very narrow basins of attraction therefore, to get this specific solution it is necessary to put precise initial conditions.

The basins of attractions for $\lambda = 2.1$ and two selected frequencies $\omega = 23\,\mathrm{rad/s}$ and $\omega = 25\,\mathrm{rad/s}$ are presented in Fig. 15a and 15b, respectively. Attractor A_1 represents C configuration and is discussed in the next section. The in-well oscillations for the I configuration are represented by attractor A_2 (lower branch of the resonance curve) and A_3 (the upper branch period solution). For $\omega = 23\,\mathrm{rad/s}$ (Fig. 15a) the period doubling is clearly visible by double A_3 points in contrast to the single point for omega $\omega = 25\,\mathrm{rad/s}$ (Fig. 15b). Basins of attraction for attractors A_1 (red colour area) and A_2 (green colour area) are vast comparing with very narrow basins of attractions of A_3 shown in a white colour area. This result demonstrates that for large oscillations, the new solution occurring due to a period doubling bifurcation has a very narrow basis of attraction. Therefore it is difficult to get this configuration experimentally. Basins for the 1-T period oscillations around $I-$ and C configurations are much wider.

The frequency response curves for further increased excitation $\lambda = 2.5$,

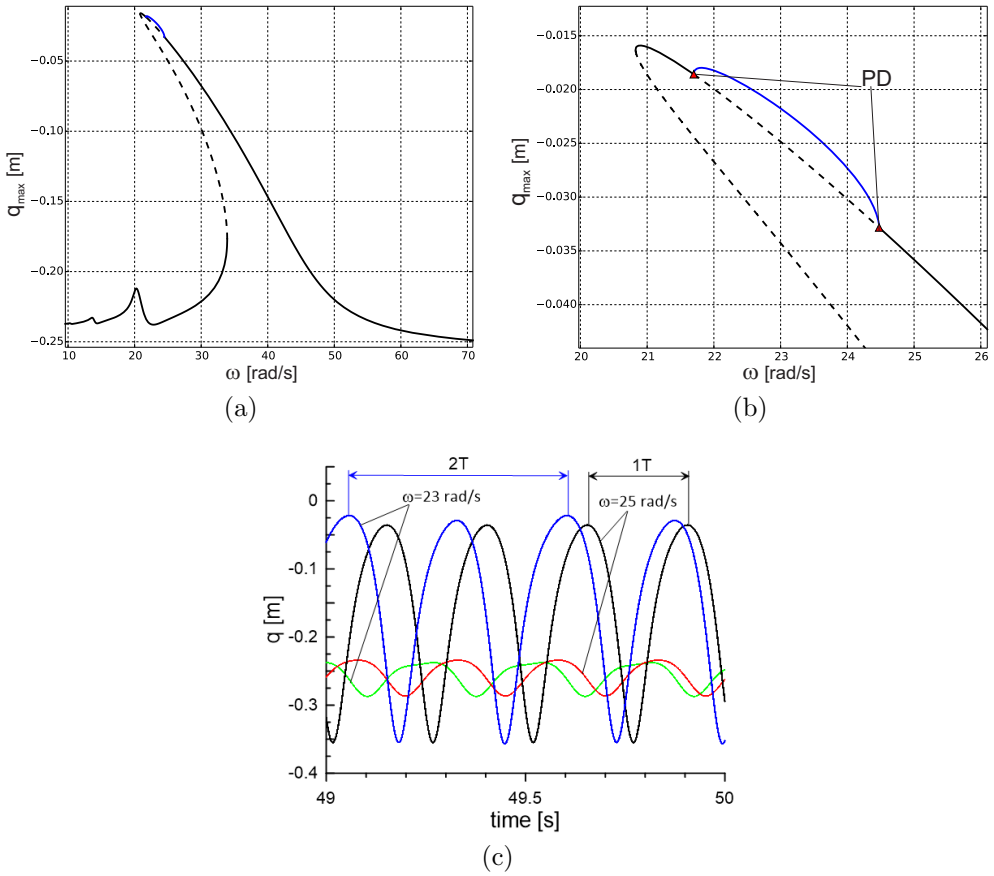

Figure 14: Resonance curves for amplitude of excitation $\lambda = 2.1$ (a), zoom of the peak with period doubling points (PD) (b) and time histories for $\omega = 23$–blue and green and $\omega = 25$–black and red (c); I-state.

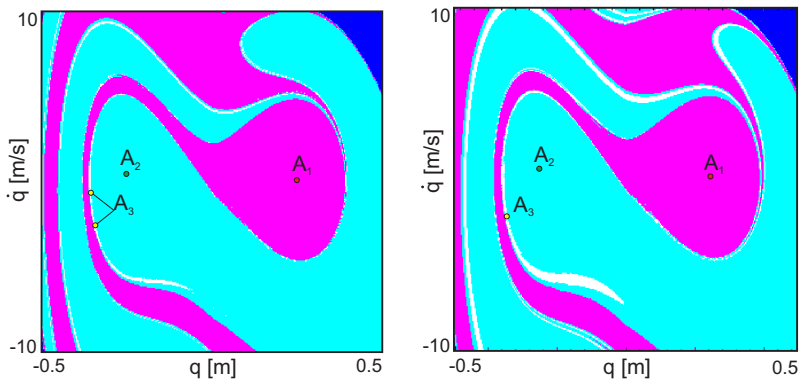

(a) $\omega = 23$. (b) $\omega = 25$.

Figure 15: Basins of attraction for $\lambda = 2.1$.

$\lambda = 3.85$, is presented in Fig. 16 for which a different bifurcation scenario is observed. For $\lambda = 2.5$ a period doubling bifurcation occurs for large amplitudes, similar to that presented in Fig. 14. However, now the period doubling bifurcation occurs earlier (for smaller amplitudes) and then after the first bifurcation a cascade of a period doubling takes place (not indicated in the figure) and the system goes to zero value (red cross) which is a limit of the I configuration domain. For $\lambda = 3.85$ the period doubling occurs again for smaller amplitudes and additional solutions occur. The additional separated solutions have been detected on the basis of the bifurcation diagram - amplitude of solution against λ parameter for fixed excitation $\omega = 50\,\mathrm{rad/s}$ (Fig. 17). The zoom in Fig. 17b indicates a branch of stable solutions which allowed computing the isola in Fig. 16b.

The detected period doubling bifurcation occurs much earlier if excitation is essentially increased, for example up to $\lambda = 5$ as presented in Fig. 18b. Furthermore, an additional superharmonic resonance zone arises next to frequency $\omega \approx 80\,\mathrm{rad/s}$ which is double the value of the natural frequency. For $\lambda = 8.5$ (Fig. 18b) the stable part of the main resonance curve is reduced, in contrast the superharmonic resonance curve increases and a period doubling bifurcation occurs on this branch. It means that two scenarios are possible to jump to the C configuration, via the cascade of a period doubling bifurcation from the main resonance or via the superharmonic resonance which starts to play an important role if excitation is increased.

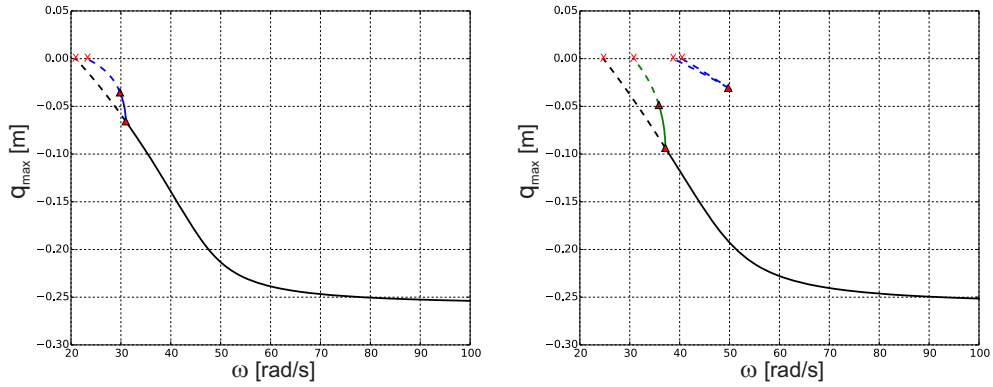

(a) $\lambda = 2.5$. (b) $\lambda = 3.85$.

Figure 16: Frequency response curves for selected amplitude of excitation, I configuration.

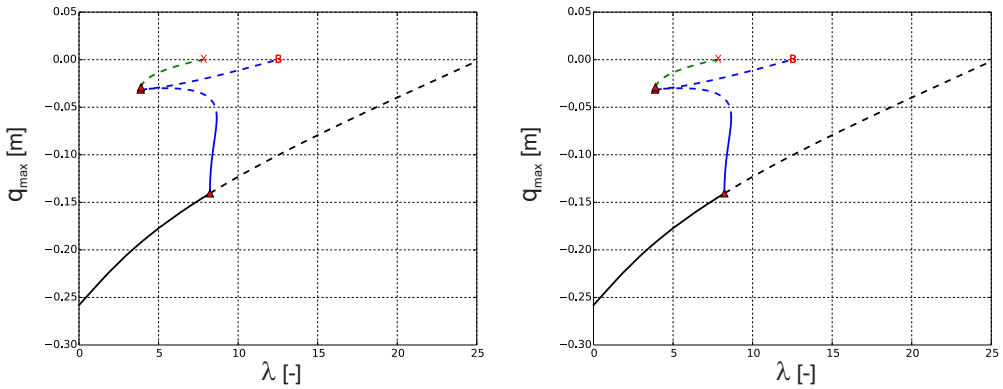

(a) General overview. (b) Zoom next to bifurcation points.

Figure 17: Bifurcation diagram against λ parameter and fixed frequency $\omega = 50\,\mathrm{rad/s}$, I configuration.

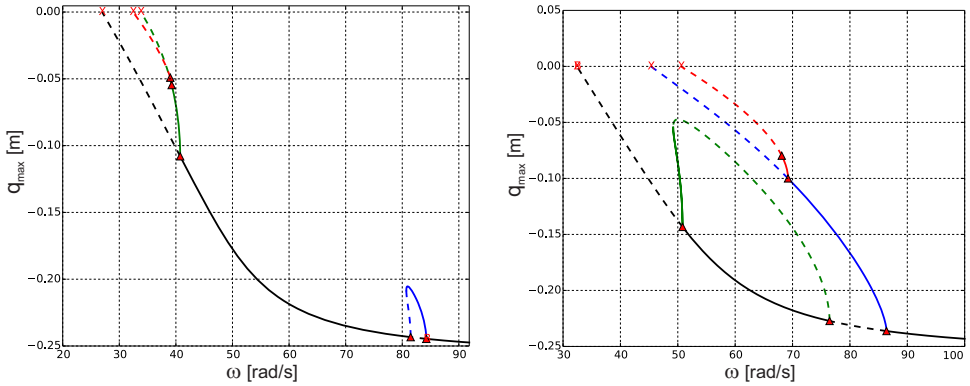

(a) $\lambda = 5$. (b) $\lambda = 8.5$.

Figure 18: Frequency response curves for selected amplitude of excitation, I configuration.

5.2. Periodic dynamics - C configuration

The analysis of the periodic response is extended to the dynamics around the C configuration. The frequency response curves for relatively small oscillations are presented in Fig.19. The curves have softening nature, similar to oscillations around the I configuration. In this case however, the softening is weaker comparing to similar excitation level of the I-configuration.

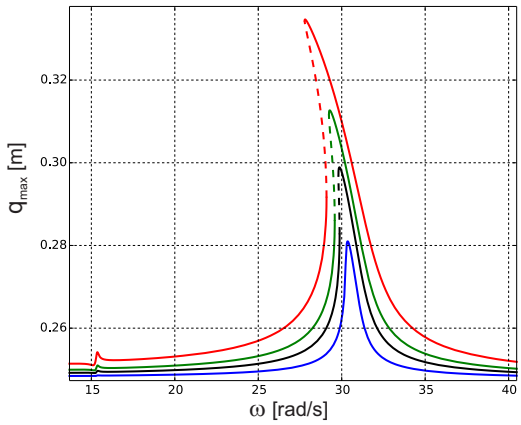

Figure 19: Resonance curves for $\lambda = 0.5$–blue, $\lambda = 1.0$–black, $\lambda = 1.5$–green, $\lambda = 2.5$–red; C configuration.

The resonance curves for larger oscillations are presented in Fig.20. The large value of excitation $\lambda = 4.5$ does not lead to a period doubling bifurcation scenario but at the amplitude peak the stable and unstable solutions replace

their positions, Fig. 20b. We note that the subharmonic resonance around $\omega \approx 15\,\mathrm{rad/s}$ arises and is clearly visible for larger oscillations. In contrast to the I-configuration the superharmonic resonance is not observed in the range of the analysed parameters.

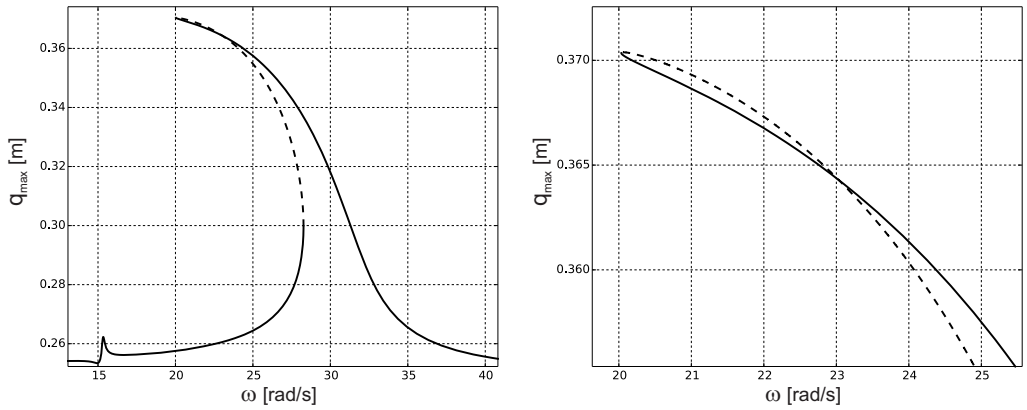

(a) Resonance curve. (b) Zoom of top amplitude zone.

Figure 20: Resonance curve for $\lambda = 4.5$, C configuration.

The period doubling bifurcation occurs for $\lambda = 5$, Fig. 21. Close to the peak loop crated by stable and unstable solutions and a new branch followed by a period doubling bifurcation arises (zoom in Fig.21b). Starting from this point a cascade of period doubling takes place (not presented in the figure). This zone is an indication for further studies of global oscillations leading to possible chaotic response with jumps between two potential wells.

A bifurcation diagram, amplitude against amplitude of excitation λ, for fixed excitation frequency $\omega = 50\,\mathrm{rad/s}$ is presented in Fig. 22. An increase of parameter λ does not change the response qualitatively in the large parameter domain: the amplitude of oscillations increases almost linearly up to very large value of $\lambda \approx 90$ (Fig. 22a). Then, the unstable branch arises going to a limit point where stable solution exists (blue line in Fig. 22a). This solution bifurcates and a cascade of period doubling takes place as presented in the enlarged zone in Fig. 22b by green and red lines.

5.3. Global dynamics - regular and chaotic motion

To detect not only local (in-well) periodic solutions the simulations for global dynamics are performed. The interest lies in determining the zone of nonlinear oscillations, including snap-through effects, where the shell may

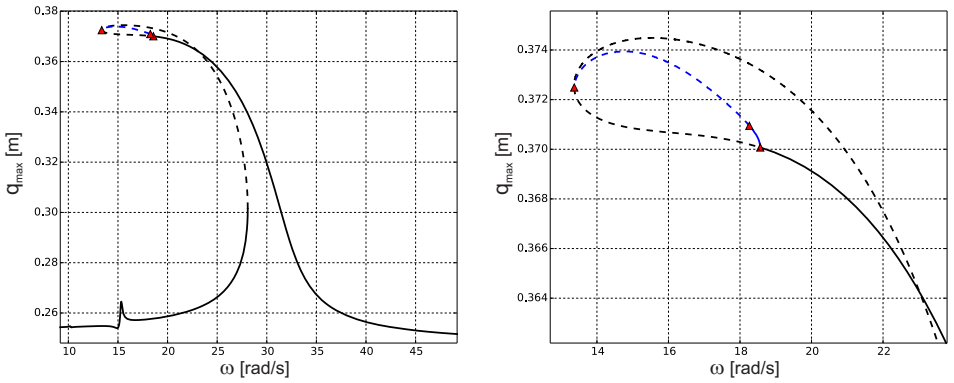

(a) Resonance curve. (b) Zoom of top amplitude zone.

Figure 21: Resonance curves for $\lambda = 5.0$, C configuration.

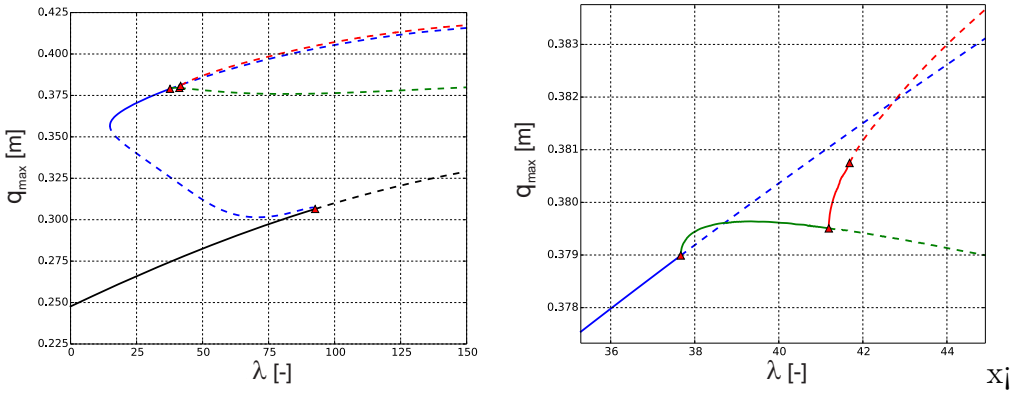

(a) General overview. (b) Zoom of bifurcation scenario.

Figure 22: Bifurcation diagram of maximal displacement against λ parameter for $\omega = 50\,\mathrm{rad/s}$, C configuration.

jump from one to another potential well or jump between both potential wells, I and C configurations. These nonlinear behaviours, either local or global, are effective for energy harvesting; moreover, their operating conditions can guide a suitable shell design.

In the following analysis the transient states are rejected and then the solution is plotted on the bifurcation diagrams with a projection equal to excitation frequency. The rejected number of transient periods is set to guarantee that a steady state is obtained. All computations are repeated starting from different initial conditions or in some cases for fixed initial conditions for better results interpretation. Starting from different initial conditions we are able to find more coexisting solutions than using the classical continuation method while for fixed initial conditions we may ensure that out-of-well oscillations are produced by the system itself.

In Fig. 23 we present the bifurcation diagram for relatively small excitations $\lambda = 1$ and $\lambda = 2.5$. For $\lambda = 1$ (Fig. 23a) only local periodic oscillations are observed, depending whether the system oscillates around the I or C configurations in the initial conditions. This is in agreement with former results presented in Sec. 5.1 and 5.2. We note that the bifurcation diagrams show a projection of the solution thus the resonance zones have a different view than those computed by a continuation technique.

For $\lambda = 2.5$ we expect to get period doubling bifurcation (see Fig. 16a) and more complex dynamics. In fact, in Fig. 23b and enlarged zone A, shown in Fig. 23c, a period doubling bifurcation is present. Varying frequency ω backward the cascade of period doubling leads to a narrow black zone which vanishes for the certain value of ω. A systematic change of initial conditions enables detecting another narrow zone of solutions, not detected by the continuation technique. The solution are presented in narrow zone B enlarged in Fig. 23d where again the period doubling scenario is observed.

To confirm the nature of motion in the zone presented in Fig. 23c and existence of all possible periodic solutions we compute basins of attractions for $\lambda = 2.5$ and $\omega = 29.3\,\mathrm{rad/s}$, Fig. 24a. Attractor A_1 represents a periodic solution around C configuration, attractor A_2 corresponds to periodic solutions around I configuration. The third attractor A_3 plotted in yellow with white basins of attraction has chaotic nature. The computed maximal Lyapunov exponent gets positive value which confirms that attractor A_3 is an in-well strange chaotic attractor, localised around the I configuration.

If excitation frequency is slightly changed up to $\omega = 30\,\mathrm{rad/s}$ the strange chaotic attractor transforms into the regular solution with a double period,

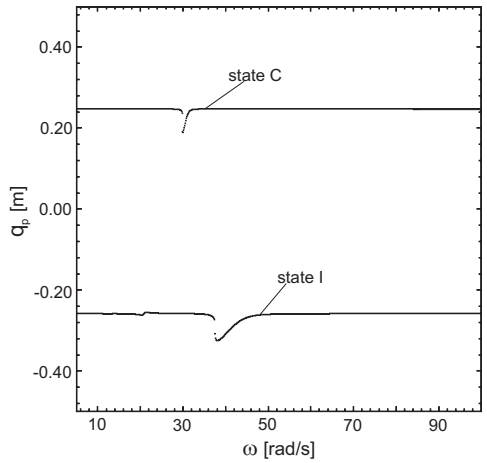

(a) $\lambda = 1.0$.

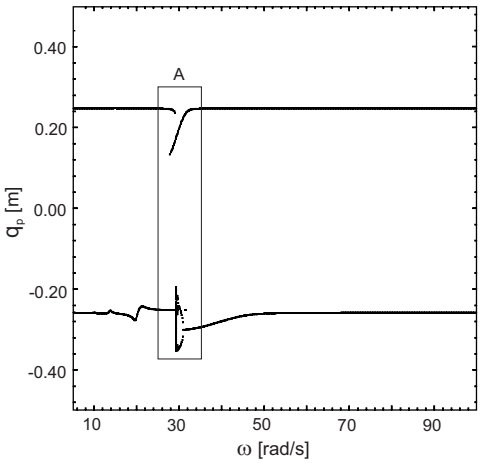

(b) $\lambda = 2.5$ (computed for 11 different initial conditions).

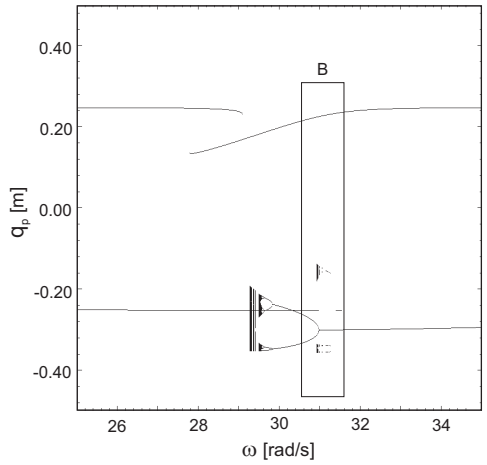

(c) Zoom of zone A.

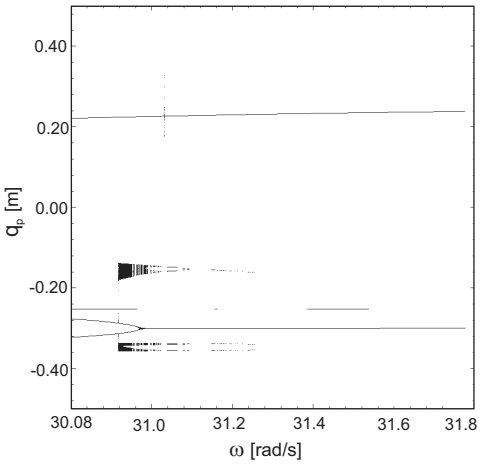

(d) Zoom of zone B.

Figure 23: Bifurcation diagrams; projected solution q against excitation frequency ω.

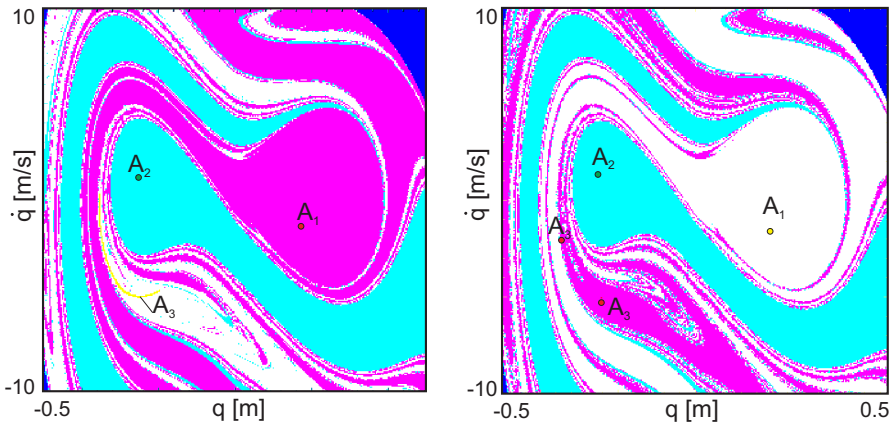

(a) $\omega = 29.3\,\mathrm{rad/s}$. (b) $\omega = 30\,\mathrm{rad/s}$.

Figure 24: Basins of attraction for $\lambda = 2.5$.

shown by double point A_3 in Fig. 24b.

In order to get double-well dynamics it is necessary to increase the amplitude of excitation λ. Bearing in mind solutions obtained in previous subsections and to keep the excitation at a more realistic level we increase its value up to $\lambda = 5$. Now the initial conditions are fixed as $q = -0.2\,\mathrm{m}, \dot{q} = 0\,\mathrm{m/s}$ and excitation frequency is varied. Such an investigation allows detecting zones with a jump to C configuration despite initial conditions located close to the I configuration. In the bifurcation diagram in Fig. 25a jumps between I and C configurations are visible. Varying frequency ω periodic solutions represented by negative values correspond to the I configuration while positive to the C configuration.

As we can see, in zones A and B indicated in Fig. 25a more complex dynamics with local or global chaotic motion is possible. This fact is presented in enlarged zones A and B in Fig. 25b and 25c, respectively. In zone A (Fig. 25b), around frequency $\omega \approx 30.5$ where double dark areas occur, oscillations with snap-through effect took place. Varying frequency backward we get periodic solutions, next we observe a first period doubling and then a cascade of a period doubling leading to chaotic oscillations. Below $\omega \approx 30.5\,\mathrm{rad/s}$ chaotic oscillations rapidly disappear.

The bifurcation diagram has been plotted for fixed initial conditions $q = -0.2\,\mathrm{m}, \dot{q} = 0\,\mathrm{m/s}$. To detect other existing solutions and to explain the bifurcation scenario we compute basins of attraction around this specific zone. We start from $\omega = 30.68\,\mathrm{rad/s}$ (Fig. 26) and then we move backward.

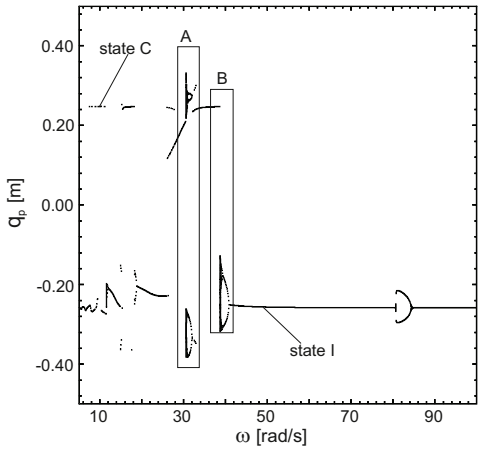

(a) General overview.

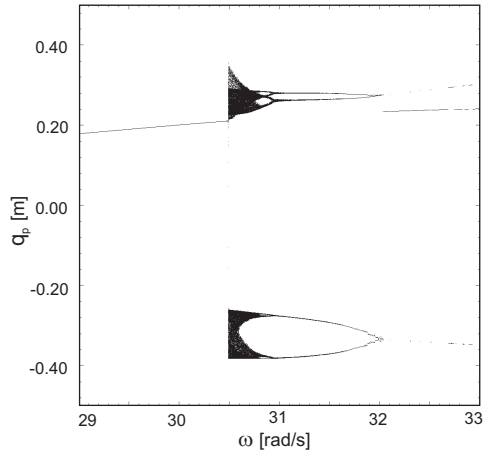

(b) Zoom of frequency zone A.

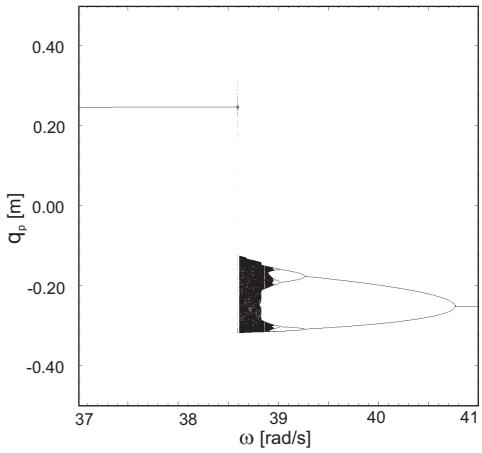

(c) Zoom of frequency zone B.

Figure 25: Bifurcation diagrams for $\lambda = 5.0$ computed for fixed initial condition $q = -0.2\,\mathrm{m}, \dot{q} = 0\,\mathrm{m/s}$.

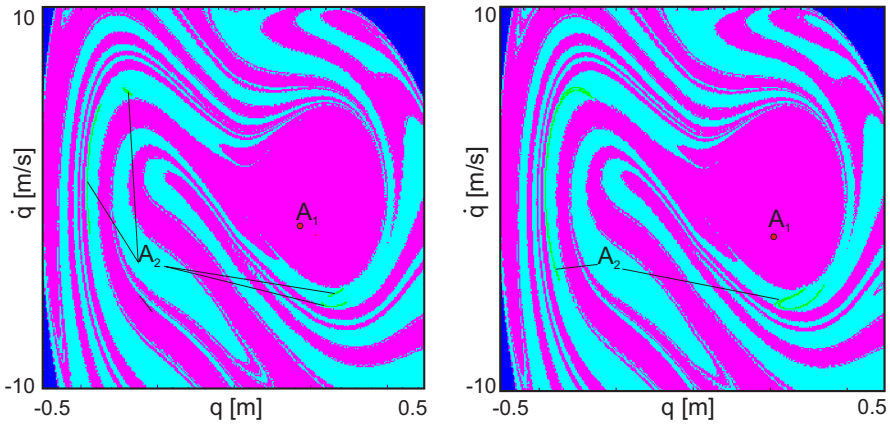

(a) $\omega = 30.68\,\mathrm{rad/s}$.

(b) $\omega = 30.52\,\mathrm{rad/s}$.

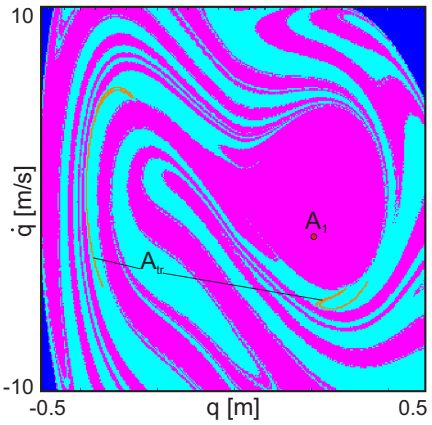

(c) $\omega = 30.51\,\mathrm{rad/s}$.

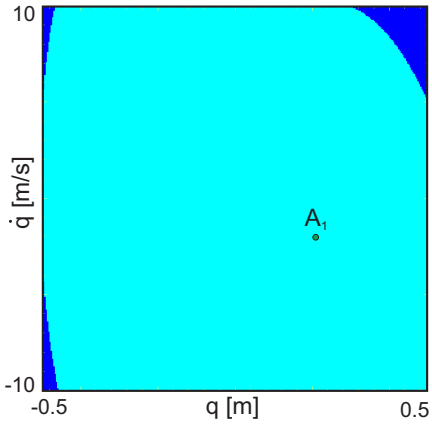

(d) $\omega = 30.49\,\mathrm{rad/s}$.

Figure 26: Basins of attraction for $\lambda = 5$.

In Fig. 26a two types of oscillations are possible, A_1 which is a periodic attractor of the C configuration with basins in red colour and the chaotic attractor A_2 composed of four small green areas with basins in light green. We note that the chaotic attractor is partially located on the negative and partially on positive part of the phase plane. This means that system oscillates globally, moving between $I-$ and C configurations. The basins of attraction computed for frequency $\omega = 30.68\,\mathrm{rad/s}$ (Fig. 26a) enabled to detect the chaotic attractor and the coexisting periodic attractor around C configuration.

Moving frequency backward the chaotic attractor is merged into two larger components as presented in (Fig. 26b) for $\omega = 30.52\,\mathrm{rad/s}$. For $\omega = 30.51\,\mathrm{rad/s}$ (Fig. 26c) it is almost touching the boundaries of basins of attractions of A_1. When the chaotic attractor touches the boundaries the boundary crisis bifurcation takes place and the chaotic attractor disappears. This effect is observed in Fig. 26c, where A_{tr} means transient attractor which disappears after long time. For $\omega = 30.49\,\mathrm{rad/s}$ the transient chaotic response does not exist any more (Fig. 26d) and just a periodic solution around the C configuration maintains. Time histories corresponding to attractors A_1 and A_2 from Fig. 26b for $\omega = 30.52\,\mathrm{rad/s}$ are presented in Fig. 27.

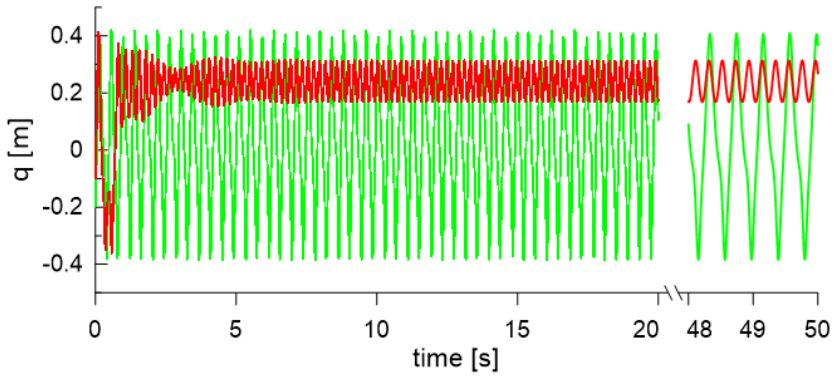

Figure 27: Time histories of regular motion around C configuration (red) and global chaotic oscillations (green) for $\lambda = 5$, $\omega = 30.52\,\mathrm{rad/s}$.

In zone B presented in Fig. 25c only local chaotic motion around I configuration is observed (dark zone around $q \approx -0.2\,\mathrm{m}$, $\omega \approx 38.6\,\mathrm{m/s}$).

The global motion with snap-through effect for $\lambda = 5$ may occur only for a very narrow frequency domain. Therefore, realization of such motion in a real application could be rather difficult. To enlarge the zones of global

oscillations a further increase of the amplitude of excitation is needed. However, limitations of a level of real excitation should be taken into account. Thus, to check the tendency we increase excitation to $\lambda = 8.5$. A bifurcation diagram computed again for fixed initial conditions $q = -0.2\,\mathrm{m}, \dot{q} = 0\,\mathrm{m/s}$ is presented in Fig. 28.

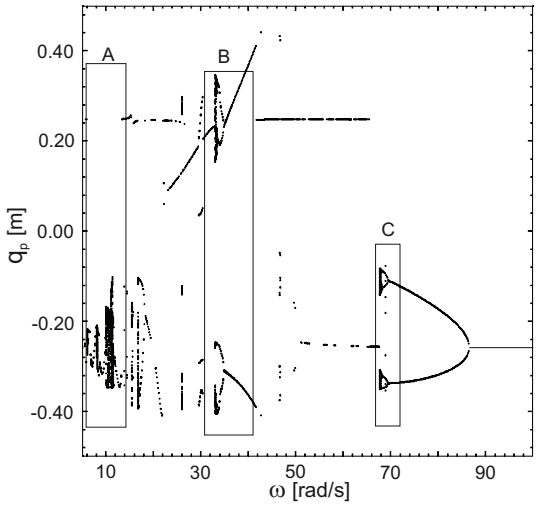

Figure 28: Bifurcation diagram for $\lambda = 8.5$ computed for fixed initial conditions $q = -0.2\,\mathrm{m}, \dot{q} = 0\,\mathrm{m/s}$; general overview with indicated frequency zones A, B and C.

For the tested frequency domain we select free sub-domains for low frequency $\omega \approx 10.0\,\mathrm{rad/s}$, middle frequency $\omega \approx 35\,\mathrm{rad/s}$ and high frequency $\omega \approx 68\,\mathrm{rad/s}$. The enlarged sub-domains are presented in Fig. 29.

For low frequency two possible solutions exist (presented in Fig. 30a for $\omega = 8.5\,\mathrm{rad/s}$): (i) periodic solution around the C configuration (red attractor A_1 with red basins) or (ii) chaotic oscillations around the I configuration (green strange chaotic attractor with light green basins).

The searched global oscillations with a snap-through between potential wells can be obtained for frequency around $\omega \approx 33\,\mathrm{rad/s}$. This motion is shown in Fig. 30b with chaotic attractor composed of two parts (A_2 in green with light green basins) for $\omega = 32.78\,\mathrm{rad/s}$ which splits into four parts for $\omega = 32.91\,\mathrm{rad/s}$ in Fig. 30c. In both cases global chaotic oscillations coexist with local periodic around C configuration (attractor A_1 in red). In contrast for the high frequency sub-domain three coexisting solutions are present in Fig. 30d, periodic oscillations around C configuration (attractor A_1 in red) and I configuration (attractor A_2 in green) exist as well. However, apart from

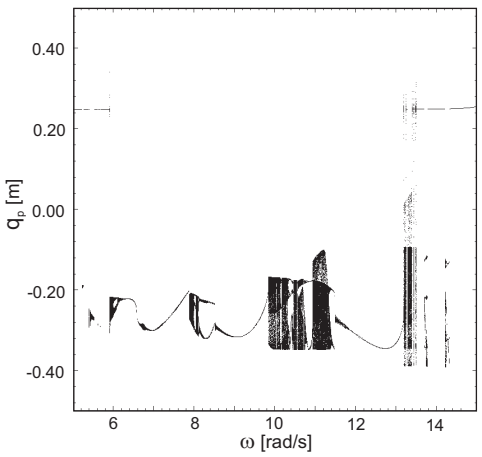

(a) Zone A.

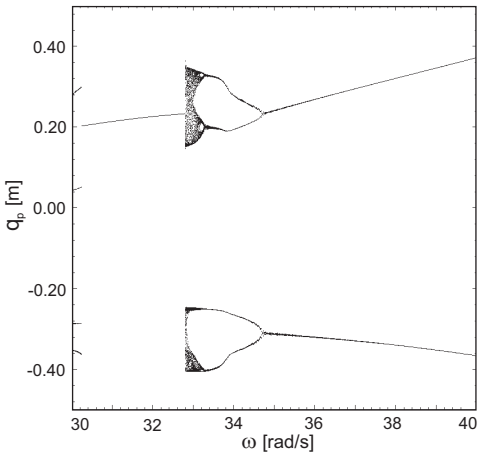

(b) Zone B.

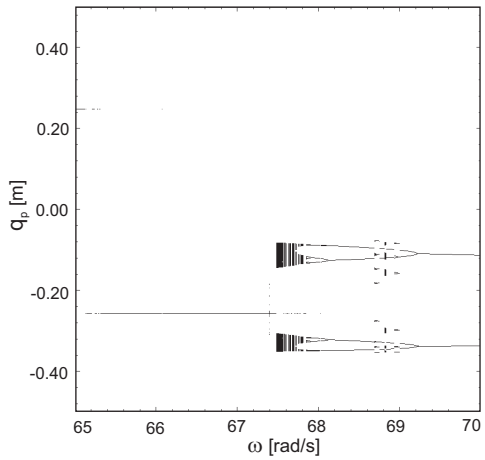

(c) Zone C.

Figure 29: Zoom of bifurcation diagrams computed for $\lambda = 8.5$ and fixed initial conditions $q = -0.2\,\mathrm{m}, \dot{q} = 0\,\mathrm{m/s}$.

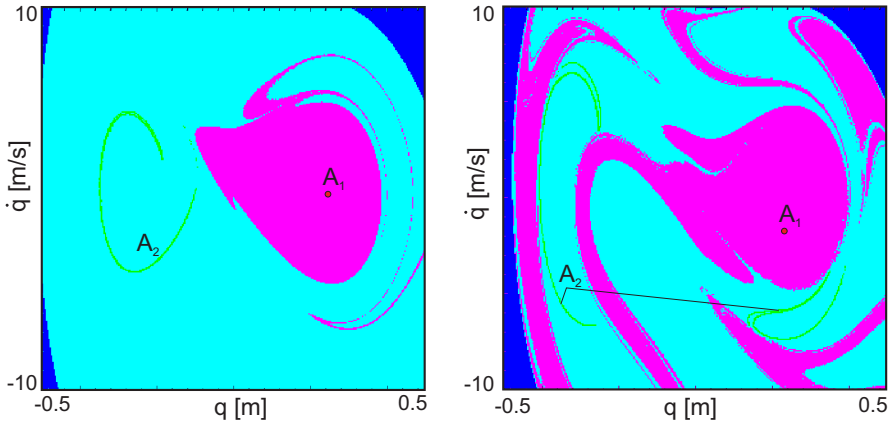

(a) $\omega = 11.2\,\mathrm{rad/s}$.

(b) $\omega = 32.78\,\mathrm{rad/s}$.

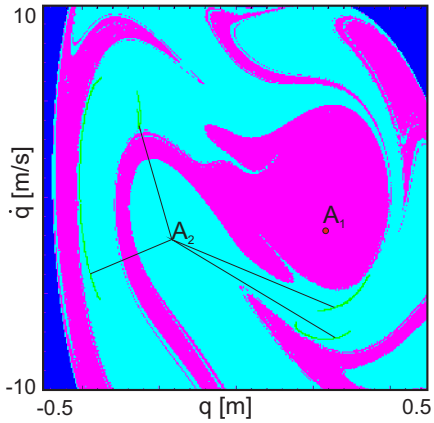

(c) $\omega = 32.91\,\mathrm{rad/s}$.

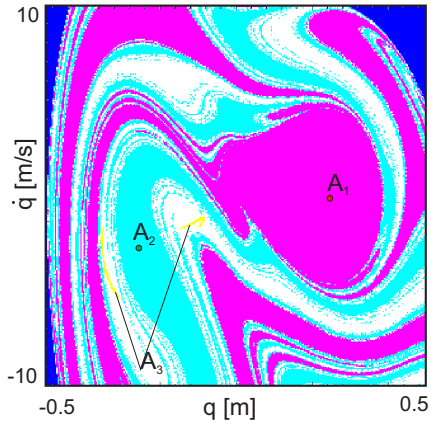

(d) $\omega = 67.50\,\mathrm{rad/s}$.

Figure 30: Basins of attraction for $\lambda = 8.5$.

two possible periodic oscillations also chaotic motion is located on negative part of the phase plane around I configuration. The strange chaotic attractor A_3 (in yellow) can be achieved if initial conditions are properly selected from basins plotted in white.

The increased amplitude of excitation does not enlarged essentially the domains of existing two-well oscillations. The local chaotic motion is present only around the I configuration for considered level of amplitude and frequency of excitation. Chaotic oscillations around the C configuration have not been obtained. This results confirm difficulties in obtaining global motion in real experimental tests. To widen the domains of two-well oscillations it is necessary to modify the shell structural parameters. This goal is a subject of future studies.

6. Concluding remarks and future work

On the basis of experimental data the nonlinear dynamics of composite bistable cantilever shells was addressed. In order to capture the observed main nonlinear features, a reduced 1DoF nonlinear oscillator with double potential well is proposed. Dictated by experimental results and FE simulations, the model extends the Duffing-Holmes equation to cubic-quintic terms.

For relatively *small oscillations* around both the shell stable configurations a nonlinear softening effect was experimentally detected. This behaviour is properly captured by the proposed model, whose resonance curves are in good agreement with experimental results; however, the large difference in shape betweeen the shell stable configurations forced a separate identification of the model parameters. Notably, an *ad-hoc* nonlinear damping model has been proved necessary to properly describe the dynamics of the shell. Indeed, the experimentally determined damping behaviour depends upon the level of excitation and it differs for the two stable configurations of the shell.

For *large oscillations*, the numerically detected cascade of period doubling bifurcations is an indicator of the transition to chaotic motion. The snap-through effect leading to global chaotic oscillations between the two shell stable configurations has been observed for relatively narrow frequency domains, regardless of the excitation amplitude value.

On the basis of these initial results, the dynamic response of this class of shells seems to promise interesting applications in the field of energy harvesting systems. Indeed, the relevant difference between the shell's stable shapes

guarantees a level of extracted energy much higher than that achieved with the symmetric stable shapes usually studied in the literature. However, for this to be possibile, it is essential to widen the frequency range where the snap-through occurs, since it triggers the switch from one configuration to the other. This call for a design strategy capable of ensuring the desired dynamic behaviour, that is, the one maximizing the energy harvesting capabilities. Such design procedure calls for simple modelling tools like the proposed 1DoF model, in which active MFC elements and relevant electrical circuits can be directly modeled; the latter aspects are a subject of the authors' ongoing research.

7. Acknowledgements

The authors acknowledge the financial support of the Programme Canaletto, Project PO19MO15 - Protocol MAE01738472019-10-09 and PPN/BIL/2018/2/00076. M. Brunetti acknowledges the support of the Italian National Group of Mathematical Physics (GNFM-INdAM).

References

[1] M. Hyer, Some observations on the cured shape of thin unsymmetric laminates, Journal of Composite Materials 15 (1981) 175–194.

[2] E. Kebadze, S. Guest, S. Pellegrino, Bistable prestressed shell structures, International Journal of Solids and Structures 41 (2004) 2801–2820.

[3] S. Daynes, K. Potter, P. Weaver, Bistable prestressed buckled laminates, Composites Science and Technology 68 (2008) 3431–3437.

[4] S. Guest, S. Pellegrino, Analytical models for bistable cylindrical shells, Proceedings of the Royal Society A: Mathematical, Physical and Engineering Sciences 462 (2006) 839–854.

[5] M. Brunetti, A. Vincenti, S. Vidoli, A class of morphing shell structures satisfying clamped boundary conditions, International Journal of Solids and Structures 82 (2016) 47–55.

[6] M. Brunetti, S. Vidoli, A. Vincenti, Bistability of orthotropic shells with clamped boundary conditions: An analysis by the polar method, Composite Structures 194 (2018) 388–397.

[7] M. Brunetti, A. Favata, S. Vidoli, Enhanced models for the nonlinear bending of planar rods: localization phenomena and multistability, Proceedings of the Royal Society A 476 (2020) 20200455.

[8] M. Brunetti, L. Kloda, F. Romeo, J. Warminski, Multistable cantilever shells: analytical prediction, numerical simulation and experimental validation, Composites Science and Technology 165 (2018) 397–410.

[9] A. Mukherjee, M. Friswell, S. Ali, A. Arockiarajan, Modeling and design of a class of hybrid bistable symmetric laminates with cantilever boundary configuration, Composite Structures 239 (2020).

[10] S. Emam, D. Inman, A review on bistable composite laminates for morphing and energy harvesting, Applied Mechanics Reviews 67 (2015).

[11] Z. Zhang, Y. Li, X. Yu, X. Li, H. Wu, H. Wu, S. Jiang, G. Chai, Bistable morphing composite structures: A review, Thin-Walled Structures 142 (2019) 74–97.

[12] C. Diaconu, P. Weaver, A. Arrieta, Dynamic analysis of bi-stable composite plates, Journal of Sound and Vibration 322 (2009) 987–1004.

[13] A. Arrieta, S. Neild, D. Wagg, Nonlinear dynamic response and modeling of a bi-stable composite plate for applications to adaptive structures, Nonlinear Dynamics 58 (2009) 259–272.

[14] A. Arrieta, S. Neild, D. Wagg, On the cross-well dynamics of a bi-stable composite plate, Journal of Sound and Vibration 330 (2011) 3424–3441.

[15] A. Senba, T. Ikeda, T. Ueda, A two-way morphing actuation of bi-stable composites with piezoelectric fibers, in: 51st AIAA/ASME/ASCE/AHS/ASC Structures, Structural Dynamics, and Materials Conference 18th AIAA/ASME/AHS Adaptive Structures Conference 12th, p. 2744.

[16] G. Vogl, M. Hyer, Natural vibration of unsymmetric cross-ply laminates, Journal of Sound and Vibration 330 (2011) 4764–4779.

[17] A. F. Arrieta, O. Bilgen, M. I. Friswell, P. Hagedorn, Dynamic control for morphing of bi-stable composites, Journal of Intelligent Material Systems and Structures 24 (2013) 266–273.

[18] A. Arrieta, G. Spelsberg-Korspeter, P. Hagedorn, S. Neild, D. Wagg, Low order model for the dynamics of bi-stable composite plates, Journal of Intelligent Material Systems and Structures 22 (2011) 2025–2043.

[19] A. Firouzian-Nejad, S. Ziaei-Rad, M. Moore, Vibration analysis of bi-stable composite cross-ply laminates using refined shape functions, Journal of Composite Materials 51 (2017) 1135–1138.

[20] Z. Wu, H. Li, M. I. Friswell, Advanced nonlinear dynamic modelling of bi-stable composite plates, Composite Structures 201 (2018) 582–596.

[21] S. Emam, Snapthrough and free vibration of bistable composite laminates using a simplified rayleigh-ritz model, Composite Structures 206 (2018) 403–414.

[22] A. Arrieta, P. Hagedorn, A. Erturk, D. Inman, A piezoelectric bistable plate for nonlinear broadband energy harvesting, Applied Physics Letters 97 (2010) 104102.

[23] D. Betts, H. Kim, C. Bowen, D. Inman, Optimal configurations of bistable piezo-composites for energy harvesting, Applied Physics Letters 100 (2012).

[24] D. Betts, H. Kim, C. Bowen, D. Inman, Static and dynamic analysis of bistable piezoelectric-composite plates for energy harvesting, in: 53rd AIAA/ASME/ASCE/AHS/ASC Structures, Structural Dynamics and Materials Conference 20th AIAA/ASME/AHS Adaptive Structures Conference 14th AIAA, p. 1492.

[25] D. Betts, C. Bowen, H. Kim, N. Gathercole, C. Clarke, D. Inman, Nonlinear dynamics of a bistable piezoelectric-composite energy harvester for broadband application, European Physical Journal: Special Topics 222 (2013) 1553–1562.

[26] P. Harris, C. R. Bowen, H. A. Kim, Manufacture and characterisation of piezoelectric broadband energy harvesters based on asymmetric bistable laminates, Journal of Multifunctional Composites 2 (2014) 113–123.

[27] M. Taki, R. Tikani, S. Ziaei-Rad, A. Firouzian-Nejad, Dynamic responses of cross-ply bi-stable composite laminates with piezoelectric layers, Archive of Applied Mechanics 86 (2016) 1003–1018.

[28] A. Lee, D. Inman, Electromechanical modelling of a bistable plate with macro fiber composites under nonlinear vibrations, Journal of Sound and Vibration 446 (2019) 326–342.

[29] M. Colin, O. Thomas, S. Grondel, É. Cattan, Very large amplitude vibrations of flexible structures: Experimental identification and validation of a quadratic drag damping model, Journal of Fluids and Structures 97 (2020) 103056.

[30] E. J. Doedel, A. R. Champneys, F. Dercole, T. F. Fairgrieve, Y. A. Kuznetsov, B. Oldeman, R. Paffenroth, B. Sandstede, X. Wang, C. Zhang, Auto-07p: Continuation and bifurcation software for ordinary differential equations (2007).